
VARIATIONAL BAYESIAN LATENT ESTIMATION WITH COMPRESSIVE AUTOENCODERS

Maud Biquard

ISAE-Supaero / CNES
31400 Toulouse, France
maud.biquard@isae-superaero.fr

Florence Genin, Christophe Latry

CNES
31400 Toulouse, France
firstname.lastname@cnes.fr

Marie Chabert

IRIT/INP-ENSEEIH
31000 Toulouse, France
marie.chabert@toulouse-inp.fr

Thomas Oberlin

ISAE-Supaero
31400 Toulouse, France
thomas.oberlin@isae-superaero.fr

ABSTRACT

Regularization of inverse problems is of paramount importance in computational imaging. The ability of neural networks to learn efficient image representations has been recently exploited to design powerful data-driven regularizers. While state-of-the-art plug-and-play methods rely on an implicit regularization provided by neural denoisers, alternative Bayesian approaches consider Maximum A Posteriori (MAP) estimation in the latent space of a generative model, thus with an explicit regularization. However, state-of-the-art deep generative models require a huge amount of training data compared to denoisers. Besides, their complexity hampers the optimization involved in latent MAP derivation. In this work, we first propose to use compressive autoencoders instead. These networks, which can be seen as variational autoencoders with a flexible latent prior, are smaller and easier to train than state-of-the-art generative models. As a second contribution, we introduce the Variational Bayes Latent Estimation (VBLE) algorithm, which performs latent estimation within the framework of variational inference. Thanks to a simple yet efficient parameterization of the variational posterior, VBLE allows for fast and easy (approximate) posterior sampling. Experimental results on image datasets BSD and FFHQ demonstrate that VBLE reaches similar performance than state-of-the-art plug-and-play methods, while being able to quantify uncertainties faster than other existing posterior sampling techniques.

1 Introduction

Image restoration tasks, such as deblurring, inpainting or super-resolution, consist in recovering a clean image x from its noisy measurement y , based on the forward model $y = Ax + w$, with A representing the degradation operator and w an additive noise term. Within the Bayesian framework, this ill-posed inverse problem is typically solved by finding the Maximum A Posteriori (MAP) estimate, solution to the problem

$$\max_x p_{X|Y}(x|y) \Leftrightarrow \min_x -\log p_{Y|X}(y|x) - \log p_X(x) \quad (1)$$

where $\log p_{Y|X}(y|x)$ is the observation log-likelihood, which is quadratic for Gaussian noise, and $-\log p_X(x)$ acts as a regularization term, promoting solutions that are most compatible with the prior distribution $p_X(x)$. Classical regularizations include total variation [1], Tikhonov regularization [2], and sparsity-promoting penalties on well-chosen representations such as wavelet bases or dictionaries [3, 4, 5].

Deep learning has led to substantial performance gains in image restoration tasks. A first category of methods directly solves the inverse problem after a supervised end-to-end training on a dataset of original-degraded image pairs related by the forward model [6, 7]. Their performance are impressive but only for the specific inverse problem considered during training. For that reason, a second category of methods aims at learning the regularization only, leveraging the

forward model to solve the inverse problem. Besides offering a better interpretability, they allow to solve a wide range of inverse problems with the same neural network.

Among them, plug-and-play (PnP) image restoration methods [8] yield excellent performance on a wide variety of image restoration tasks. These methods classically use splitting algorithms, such as ADMM [8, 9] or HQS [10, 11], that separately handle the data term and the regularization term in the optimization problem (1). Their key concept is to use Gaussian denoisers [12], and in particular deep denoisers [13] in place of the proximal operator of the regularization. More recently, the introduction of generative denoisers, such as denoising diffusion models [14, 15], within the PnP framework, has demonstrated remarkable performance in solving inverse problems [16, 17, 18].

A more direct way to learn the regularization consists in estimating the data distribution within generative models. This line of work, referred to as latent optimization in the following, seeks the inverse problem solution in the latent space of a generative model. Specifically, given a generative model G which has been trained on a dataset of ideal images, the seminal work [19] computes a MAP estimate in its latent space by solving the following optimization problem using gradient descent:

$$\max_z p_{Z|Y}(z|y) \Leftrightarrow \min_z -\log p_{Y|Z}(y|z) - \log p_Z(z), \quad (2)$$

where z is the latent variable to be optimized, $p_Z(z)$ is the generative latent prior and $p_{Y|Z}(y|z) = p_{Y|X}(y|G(z))$, that is G is considered as a deterministic transformation from the latent to the image space. The original approach introduced in [19] is efficient for solving severely ill-posed inverse problems on images lying on a low-dimensional manifold, such as centered close-ups on human faces. Unfortunately, the manifold constraint $x = G(z)$ too strongly restricts the solution space when dealing with images lying on a high-dimensional manifold, which is the case for highly diverse and/or non-structured images, or when solving less severely ill-posed inverse problems. To address this limitation, [20, 21] permit small deviations from the generative manifold while [22, 23, 24] propose to jointly optimize x and z using splitting algorithms. Solving eq. (2) using Normalizing Flows (NF) [25] is also an option as it ensures the accessibility of any element in the image space [26, 27]. Even so, the quality of the solution remains highly dependent on the generative model. Unfortunately, the use of very deep state-of-the-art generative models makes the optimization of eq. (2) problematic. Indeed, the gradient descent often gets trapped in poor local minima [28] and it can be regarded as too computationally demanding for restoring a single image. Moreover, the training of very deep generative models require a lot of ideal images, which might not be accessible in some application contexts. In order to circumvent gradient descent, [22] uses the encoder of a variational autoencoder (VAE) as a stochastic approximate of the generative model posterior in an alternate optimization scheme on (x, z) , while [29] obtains promising performance by extending this approach to hierarchical VAEs [30], at the cost of additional image restoration hyperparameters.

All the above mentioned methods only provide a single point estimate of the inverse problem solution. However, many applications require an estimation of the confidence behind this solution. To this end, several Bayesian methods enable to sample the posterior distribution $p_{X|Y}(x|y)$ of the inverse problem solution. Some methods yield stochastic solutions to the inverse problem, relying, for instance, on the implicit prior provided by Gaussian denoisers [31] or exploiting diffusion model properties [18]. However, posterior sampling is then computationally expensive since the inverse problem must be solved for each sample generation. In this regard, Markov Chain Monte Carlo (MCMC) can lead to more effective techniques. In particular, [32] proposes to use Unadjusted Langevin Algorithm (ULA) to solve imaging inverse problems. Building on this, PnP-ULA [33] approximates the log-likelihood gradient in ULA by employing a Gaussian denoiser in a PnP framework. NF-ULA[34] directly approximates this gradient using normalizing flows while [35] uses a MCMC sampling scheme in the latent space of a generative model. Many of these methods offer theoretical convergence guarantees towards the actual posterior distribution. However it requires in practice many iterations which makes the restoration computationally heavy, despite recent attempts to speed up Markov chain convergence [36, 37]. Additionally, convergence is conditioned to the tuning of sensitive hyperparameters. Consequently, these methods often struggle to reach the state-of-the-art performance and computational efficiency achieved by their point estimate counterparts, although yielding valuable uncertainty quantification.

Focusing on latent optimization methods, this paper addresses the issues arising when dealing with diverse or non-structured images. Moreover, taking benefit of the latent framework, the proposed approach offers efficient means for posterior sampling. Hence, our contribution is twofold. First, we propose compressive autoencoders (CAEs) [38] as an alternative to state-of-the-art generative models for latent optimization methods. We consider in particular CAEs with a hyperprior [39], which yield excellent results in compression and can be seen as VAEs with an adaptive latent prior. In addition, they are significantly smaller than state-of-the-art generative models. On one hand, their adaptability allows to properly regularize inverse problems on non-structured images. On the other hand, their light structure makes the latent optimization using gradient descent [19] both scalable and effective. Second, we introduce the Variational Bayes Latent Estimation (VBLE) algorithm which estimates the latent posterior $p_{Z|Y}(z|y)$ by variational inference, leveraging CAE characteristics to design a simple yet efficient approximation of $p_{Z|Y}(z|y)$. In this way, VBLE enables to estimate the posterior distribution with negligible additional computational cost.

We conduct a comprehensive set of experiments on FFHQ [40] and BSD [41] datasets, comprising three different inverse problems: deblurring, single image super resolution (SISR) and inpainting. The proposed approach yields competitive image restoration results compared to state-of-the-art methods. It additionally offers relevant posterior sampling abilities compared to MCMC methods, with an algorithm being significantly faster.

2 Background

2.1 Variational autoencoders

VAEs are composed of an encoder, known as the inference model as it approximates the unknown posterior distribution, and of a decoder used as a generative model [42]. Both are neural networks, whose weights, ϕ and θ respectively, are learned using variational inference [43]. Let the image x depend on a latent variable z according to the following generative model:

$$p_\theta(x, z) = p_\theta(x|z)p_\theta(z). \quad (3)$$

$p_\theta(z)$ is typically a simple distribution, often chosen as $\mathcal{N}(0, I)$, while $p_\theta(x|z)$ represents the distribution learned by the decoder. The posterior distribution, defined as

$$p_\theta(z|x) = \frac{p_\theta(x|z)p_\theta(z)}{\int_z p_\theta(x|z)p_\theta(z)} \quad (4)$$

is often intractable and is approximated by $q_\phi(z|x)$, the inference model produced by the VAE encoder.

The weights θ and ϕ are learned during the training of the VAE by maximizing the Evidence Lower Bound (ELBO):

$$\mathcal{L}_{\theta, \phi}(x) = \log p_\theta(x) - KL(q_\phi(z|x)||p_\theta(z|x)) \quad (5)$$

where KL denotes the Kullback-Leibler divergence, measuring the distance between distributions. Hence, by maximizing the ELBO on a dataset \mathcal{D} containing several images x , the log-likelihood of \mathcal{D} is maximized, while the distance between the approximate and true posterior distributions is minimized. However, this version of the ELBO is intractable and can be rewritten as follows:

$$\mathcal{L}_{\theta, \phi}(x) = \mathbb{E}_{q_\phi(z|x)} [\log p_\theta(x|z)] - KL(q_\phi(z|x)||p_\theta(z)). \quad (6)$$

It consists of two terms. The first one is a data fidelity term which ensures a good reconstruction of the input x by the autoencoder. The second one encourages the latent space to match the shape of the prior distribution $p_\theta(z)$. Leveraging the reparameterization trick [42], Stochastic Gradient Variational Bayes (SGVB) estimates can be derived from the ELBO to update (θ, ϕ) .

2.2 Variational compressive autoencoders

Machine learning and especially deep learning have raised a significant interest in the lossy image compression community. In the widespread transform coding framework, the image is transformed, the obtained image representation is quantized and subsequently compressed using a lossless entropy encoder [44]. The more decorrelated and sparse the transform is, the more effective the compression becomes. Several reference model-based methods use the wavelet transform [45] while state-of-the-art deep learning methods use data-dependent transforms provided by the encoder part of a compressive autoencoder (CAE) [38, 39, 46, 47]. CAEs are learned by minimizing a rate-distortion trade-off $\mathcal{L} = \text{Rate} + \alpha \times \text{Distortion}$ [38, 39]. On one hand, the quantization introduces distortion between the original and the decompressed image. This distortion is typically measured by the Mean Squared Error (MSE) between the network input and output. On the other hand, the entropy encoder design assumes a prior distribution or so-called entropy model p for the quantized latent representation, denoted by z in the following. However, z actual distribution, denoted by q , generally differs from p . The rate is approximated by the Shannon cross entropy: $\text{Rate} = \mathbb{E}_{z \sim q} [-\log_2 p(z)]$. This value is minimized when $p = q$, that is when the rate corresponds to the information entropy.

A specificity of CAE training comes from the fact that quantization is non-differentiable. It is thus approximated during training by the addition of a uniform noise, which classically models quantization noise [48]. This noise is akin to the noise introduced during the training of a VAE in the generative framework. In the following, we denote by \bar{z} the representation before the quantization. The latent variable z is thus a noisy version of \bar{z} . Furthermore, state-of-the-art CAEs incorporate a hyperprior [39, 46, 49]. This additional autoencoder takes \bar{z} as input and estimates z 's mean μ^z and standard deviation σ^z , as illustrated in Fig. 1. The prior on z is then defined as the \bar{z} -dependent factorized distribution $\prod_k \mathcal{N}(\mu_k^z, (\sigma_k^z)^2)$ convolved by a uniform distribution to align with quantization. The hyperprior introduces another latent variable h , of much smaller dimension than z . h is also quantized, entropy coded and transmitted.

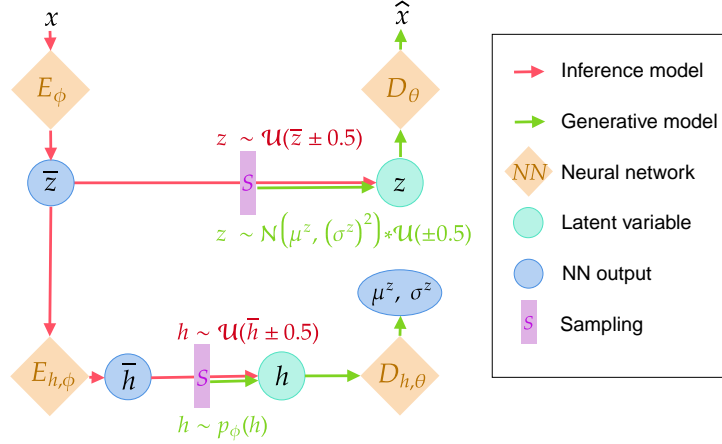


Figure 1: Structure of a compressive autoencoder with hyperprior as in [39]. All mentioned distributions are factorized, in particular $\mathcal{N}(\mu^z, (\sigma^z)^2) * \mathcal{U}(\pm 0.5) = \prod_k [\mathcal{N}(\mu_k^z, (\sigma_k^z)^2) * \mathcal{U}(-0.5, 0.5)]$.

CAEs can be formulated as VAEs [38, 39], with particular generative and inference models. Consider the following generative model, corresponding to a CAE with a hyperprior:

$$p_\theta(x, z, h) = p_\theta(x|z)p_\theta(z|h)p_\theta(h) \text{ with } p_\theta(x|z) = \prod_k \mathcal{N}(x_k; D_\theta(z)_k, \frac{1}{2\alpha \log(2)}),$$

$$p_\theta(z|h) = \prod_k \left[\mathcal{N}(z_k; \mu_k^z, (\sigma_k^z)^2) * U(z_k; [-\frac{1}{2}, \frac{1}{2}]) \right] \text{ and } p_\theta(h) = \prod_k p_\psi(h_k) \quad (7)$$

where D_θ represents the decoder part of the autoencoder, and p_ψ denotes a factorized parametric prior with weights ψ learned during training. Consider also the following inference model:

$$q_\phi(z, h|x) = q_\phi(z|x, h)q_\phi(h|x) \text{ with } q_\phi(z|x, h) = \prod_k U(z_k; [\bar{z}_k - \frac{1}{2}, \bar{z}_k + \frac{1}{2}])$$

$$\text{and } q_\phi(h|x) = \prod_k U(h_k; [\bar{h}_k - \frac{1}{2}, \bar{h}_k + \frac{1}{2}]). \quad (8)$$

Then, the ELBO from eq. (6), expressed for a hierarchical VAE with two latent variables, corresponds to the rate-distortion loss, up to a $\log(2)$ factor:

$$\mathcal{L}(x) = \mathbb{E}_{q_\phi(z, h|x)} [\log q_\phi(z, h|x) - \log p_\theta(x|z, h) - \log p_\theta(z, h)] \quad (9)$$

$$\propto 0 + \log(2)(\alpha \text{Distortion}(x, z) + \text{Rate}(z, h)).$$

Note that α controls the rate-distortion tradeoff, which is similar to the KL-data fidelity tradeoff for VAE that is generally controlled by a γ parameter assuming a Gaussian decoder of variance γ^2 [50].

Furthermore, state-of-the-art CAEs combine a second autoencoder with an autoregressive part to design an improved hyperprior [46, 47]. In this case, CAEs cannot be entirely seen as VAEs, although their formulation stay close.

Finally, CAEs are powerful neural networks, while remaining often scalable, as they are to be used in embedded systems [51]. In particular, these networks use a parametric activation function, known as Generalized Divisive Normalization [52] (GDN), which, compared to classical activation functions, affords an equivalent approximation capacity for natural images with far shallower networks.

3 Contributions

3.1 Regularization with compressive autoencoders

We claim that CAEs, introduced in Sec. 2.2, are good candidates to be used when restoring images with latent optimization methods. First, they can be viewed as VAEs and may be employed similarly. Second, they remain

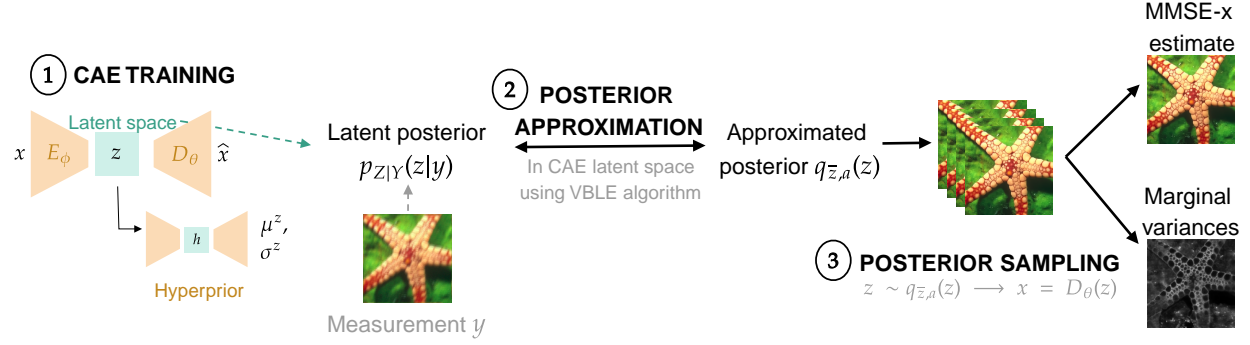


Figure 2: Overview of the image restoration process. First, a compressive autoencoder (CAE) is trained on a dataset of ideal images. Then, to restore a degraded image y , the latent posterior $p_{Z|Y}(z|y)$ is approximated using variational inference, and finally, the approximated posterior $q_{\bar{z},a}(z)$ is sampled in order to compute an MMSE estimate of the solution as well as uncertainties.

relatively light as their structure has been optimized for embedded image processing, enabling the use of gradient descent to compute the MAP- z estimate of eq. (2). Last, the hyperprior offers a flexible z -adaptive latent prior that better models the true latent distribution than typical VAE priors. Therefore, under the formalism of Sec. 2.2 summarized in Fig. 1, the MAP- z estimate for CAEs can be formulated as:

$$z^* = \arg \min_z \|AD_\theta(z) - y\|_2^2 + \lambda \text{Rate}(z, E_{h,\phi}(z)) \quad (10)$$

where $\text{Rate}(z, h) = -\log_2 p_\theta(z, h)$ and $E_{h,\phi}(z)$ denotes the output of the hyperencoder. Note that, in a proper MAP framework, both z and h should be optimized, with $-\log p_\theta(z, h) = \lambda \text{Rate}(z, h)$. As h is low-dimensional and does not significantly impact the rate, we choose the approximation $h = E_{h,\phi}(z)$. We show, in the ablation study provided in the supplementary material, that this approximation does not impact the algorithm performance.

3.2 Variational Bayes Latent Estimation (VBLE)

We still assume that $p_{Y|Z}(y|z) = p_{Y|X}(y|D_\theta(z))$. Recall that Bora et al. [19] method to solve inverse problems yields a MAP estimate $\arg \max_z p_{Z|Y}(z|y)$ in the latent space. Unlike this deterministic approach resulting in a point estimate, we wish to approximate $p_{Z|Y}(z|y)$ through variational inference, leveraging VAEs and CAEs latent structure to propose a simple posterior parameterization. Hence, we present a stochastic version of eq. (10), termed Variational Bayes Latent Estimation (VBLE), which is illustrated in Fig. 3. It consists in performing variational inference with the following parametric families:

$$\begin{aligned} E_{\bar{z},a} &= \{q_{\bar{z},a}(z) | \bar{z}, a \in \mathbb{R}^{C \times M \times N}, a > 0\} \\ \text{with } q_{\bar{z},a}(z) &= \prod_k \mathcal{U}(z_k; [\bar{z}_k - \frac{a_k}{2}, \bar{z}_k + \frac{a_k}{2}]) \quad (\text{CAE case}), \\ q_{\bar{z},a}(z) &= \prod_k \mathcal{N}(z_k; \bar{z}_k, a_k^2) \quad (\text{VAE case}). \end{aligned}$$

Note that we detail both CAE and VAE frameworks, as VBLE can be applied with both networks. These parametric families are based on the same distribution than the inference encoder distribution $q_\phi(z|x)$, *i.e.* uniform for CAEs and Gaussian for VAEs. Their parameters are the mean latent representation \bar{z} , and an additional a parameter with the same dimensions as \bar{z} , which models the uncertainty related to each coefficient of z .

Hence, employing a similar framework as the VAE training procedure described in Sec. 2.1, we maximize the ELBO:

$$\arg \max_{\bar{z},a} \mathcal{L}_{\bar{z},a} = \arg \max_{\bar{z},a} \mathbb{E}_{q_{\bar{z},a}(z)} [\log p_{Y|Z}(y|z) + \log p_\theta(z) - \log q_{\bar{z},a}(z)] \quad (11)$$

with $\log p_\theta(z)$ being the log-likelihood of the latent prior, that is in particular $\log \mathcal{N}(z; 0, I)$ for a traditional VAE, and $\log(2) \text{Rate}(z, E_{h,\phi}(\bar{z}))$ for a CAE with a hyperprior, as introduced in eq. (10). Note that $\log q_{\bar{z},a}(z) = -\sum_k \log a_k$ up to a constant in both Gaussian and uniform cases. We can then use the following reparameterization, for $z \sim q_{\bar{z},a}(z)$,

$$z = \begin{cases} \bar{z} + a \odot \epsilon \text{ with } \epsilon \sim \prod_k \mathcal{U}(\epsilon_k; [-\frac{1}{2}, \frac{1}{2}]) & (\text{CAE case}) \\ \bar{z} + a \odot \epsilon \text{ with } \epsilon \sim \mathcal{N}(0, I) & (\text{VAE case}) \end{cases}$$

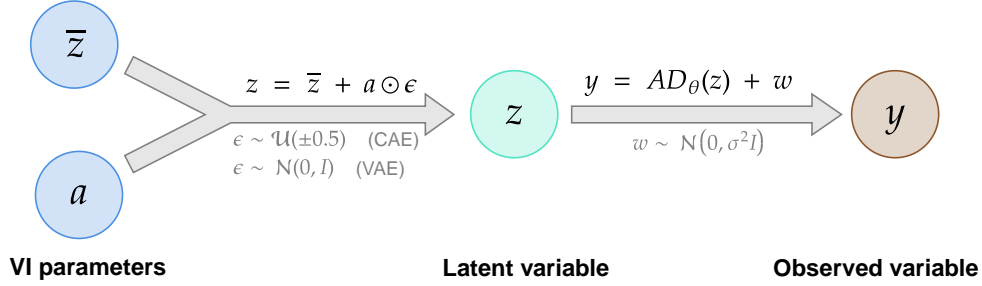


Figure 3: Variational Bayes Latent Estimation (VBLE) graph. VI stands for Variational Inference.

where \odot denotes the Hadamard, point-wise product between two tensors. Hence, the expectation in eq. (11) can be taken on ϵ using the reparametrization trick [42]. Therefore, a SGVB estimate of the ELBO can be derived, leading to algorithm 1.

Algorithm 1 Variational Bayes Latent Estimation

Require: $\bar{z}_0 \in \mathbb{R}^{C \times M \times N}$, $a_0 \in \mathbb{R}^{C \times M \times N} = (1)_{i,j,t}$, $k = 0$, $\eta > 0$

while not convergence do

$$z \sim q_{\bar{z}_k, a_k}(z)$$

$$\begin{pmatrix} \bar{z}_{k+1} \\ a_{k+1} \end{pmatrix} = \begin{pmatrix} \bar{z}_k \\ a_k \end{pmatrix} - \eta \nabla_{\bar{z}, a} \left[-\log p_{Y|Z}(y|z) - \log p_\theta(z) + \log q_{\bar{z}, a}(z) \right]$$

$$k = k + 1$$

end while

return $(\bar{z}^*, a^*) = (\bar{z}_k, a_k)$

Hence, given the optimal parameters (\bar{z}^*, a^*) , the distribution $q_{\bar{z}^*, a^*}(z)$ is supposed to approximate the posterior $p_{Z|Y}(z|y)$. Then, two point estimates can be derived for the restored image:

$$x_{MMSE-z}^* = D_\theta(\bar{z}^*), \quad (12)$$

$$x_{MMSE-x}^* = \frac{1}{L} \sum_{i=1}^L D_\theta(z_i) \text{ with } z_i \sim q_{\bar{z}^*, a^*}(z_i). \quad (13)$$

Both MMSE-x and MMSE-z estimates are relevant and can be used in practice.

3.3 Discussion and position to related works

First, it is worth noting that this variational framework does not increase the restoration time compared to its deterministic counterpart MAP-z [19]. Indeed, after convergence of VBLE, sampling from the approximate posterior is fast since it only requires forward passes through the decoder, which can be parallelized within batches. Compared to other existing posterior sampling methods to solve inverse problems, MCMC techniques [33, 35] enable to sample from the true posterior instead of an approximation, but these methods require a substantial number of iterations, making them far slower than VBLE.

Concerning variational inference methods, they have been widely used to approximate inverse problem posterior distributions [43, 53]. But the approaches which combine variational inference with deep generative modelling are essentially designed in a (semi-)supervised manner to solve a specific inverse problem [53, 54, 55], while VBLE is able to solve different inverse problems with the same network. Then, latent optimization methods [19, 22, 23] yield, up to our knowledge, only punctual solutions, except from Holden et al. [35] which, however, is an MCMC method.

Regarding the use of CAEs as regularizers, the relationship between CAEs and VAEs have been established in the literature [38, 56]. But, up to our knowledge, this is the first time that CAEs are used as priors for image restoration tasks. Although CAEs are not as deep as state-of-the-art hierarchical VAEs and may not exhibit the same performance for image generation, we believe they make appropriate priors for image restoration. In particular, the parameter α , which tunes the rate-distortion trade-off, provides additional flexibility and can be adjusted for a given inverse problem.

4 Numerical experiments

In this section, we evaluate the performance of VBLE using CAEs and compare the results with state-of-the-art baselines. We first detail the experimental setup, and then present the results on two datasets. The first one, FFHQ, is highly structured and thus well-suited for generative models, whereas the second one, BSD, contains natural images with more diversity. Regarding the baselines, we will focus on methods based on generative models for the former, and denoising networks for the latter. Finally, we assess the quality of our proposed approximate posterior compared to MCMC methods.

4.1 Experimental setup

Inverse problems. All experiments in this section are performed on subsets of BSD500 [41] and FFHQ [40] test datasets, both subsets composed of 47 images of size 256×256 . VBLE and the baselines are evaluated on three inverse problems: deblurring, single image super resolution (SISR), and inpainting. For deblurring, two Gaussian kernels of standard deviation $\sigma_{blur} \in \{1, 3\}$ are tested as well as a motion blur kernel, for several Gaussian noise levels. We consider the noiseless case for SISR and inpainting with random masks, and a small amount of noise is added for inpainting with structured masks. SISR $\times 2$ and $\times 4$ is conducted with bicubic downsampling. We employ a 50% random mask for inpainting experiments with random masks. For inpainting with structured masks, custom masks are designed on 5 test images of each dataset.

Metrics. We use three metrics to measure the discrepancy between the restored and ground truth images: Peak Signal-to-Noise Ratio (PSNR), Structural SIMilarity [57] (SSIM) and Learned Image Patch Similarity [58] (LPIPS). The PSNR derives from the pixel-wise mean-squared error, while SSIM and LPIPS are respectively classical and deep learning-based perceptual metrics.

Compressive autoencoder architectures. We employ pretrained networks from the compressAI [59] library at different bitrates. We choose Cheng et al. [47] model, which is a CAE with an hyperprior combining a second autoencoder with an autoregressive model, yielding state-of-the-art compression results. The networks from compressAI are pretrained on natural images. We finetune them for about 100k iterations on BSD and FFHQ train datasets.

VBLE parameter settings. For VBLE using CAEs, the network with the most appropriate bitrate needs to be chosen for each inverse problem. We have trained models at 7 different bitrates. The bitrate parameter α to choose, as well as the regularization parameter λ are tuned by a grid search algorithm on a defined 3 image validation set for each dataset. The other parameters are fixed, in particular, we use Adam optimizer with learning rate 0.1 during 1000 iterations for all restoration tasks. Lastly, the MMSE-x estimate is used for all comparisons as it yielded the best results.

Detailed experimental settings are given in the supplementary material, as well as extended FFHQ and BSD experiments and an ablation study about VBLE variants and hyperparameters.

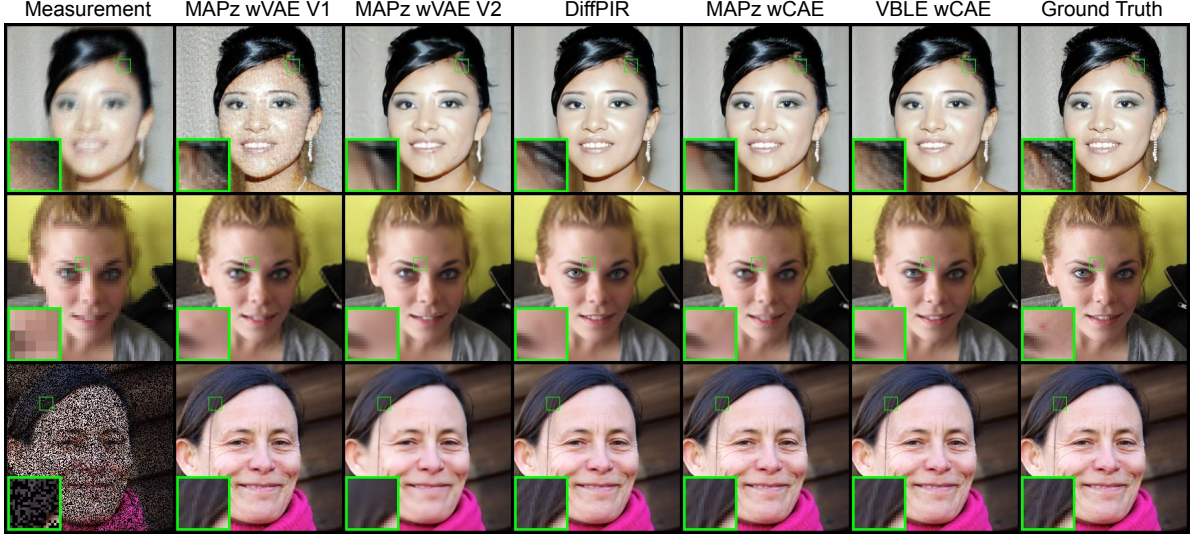
4.2 FFHQ experiments

First, we demonstrate the relevance of VBLE using CAEs for restoring highly structured face images from FFHQ dataset. To assess the effectiveness of both the CAE architecture and VBLE algorithm, we provide restoration results with VBLE (denoted as VBLE wCAE in the experiments) and also with its deterministic counterpart MAP-z using the same CAE (denoted as MAP-z wCAE).

We compare our method to the latent optimization approach Bora and al. [19] (denoted as MAP-z wVAE), which seems a natural baseline for us, as well as the state-of-the-art diffusion-based method DiffPIR [18]. For DiffPIR, we use an available FFHQ pretrained diffusion model [60]. For Bora and al. method, we train two vanilla VAE models on FFHQ. VAE-V1 and V2 are two single latent variable VAEs without and with hyperprior, with a classical convolutional structure, with approximately the same number of parameters than the CAE and the same latent dimension. Although more elaborate VAEs are likely to perform better as long as their size do not hamper the latent optimization, here we aim to assess the benefit of the CAE architecture, with its specific hyperprior. Hence we choose to compare with VAEs having similar complexity. More details on these architectures are given in supplementary material.

Quantitative results on FFHQ along with a visual comparison are provided in Tab. 1 and Fig. 4. First, the use of VBLE algorithm instead of a deterministic gradient descent not only enables posterior sampling but also enhances point estimation results, as VBLE with CAE yields better metrics than MAP-z with CAE and tends to exhibit sharper images. Then, Bora’s method MAP-z with VAEs are outperformed by VBLE, both quantitatively and qualitatively. VAE-V1 seems to lack structure while VAE-V2 lacks high frequencies, demonstrating the interest of the CAE structure and its hyperprior. Compared to DiffPIR, VBLE exhibits better PSNR and SSIM, and slightly lower LPIPS scores, which

FFHQ Method	Deblur (motion)			SISR $\times 4$			Inpainting (random)		
	PSNR \uparrow	LPIPS \downarrow	SSIM \uparrow	PSNR \uparrow	LPIPS \downarrow	SSIM \uparrow	PSNR \uparrow	LPIPS \downarrow	SSIM \uparrow
VBLE wCAE	32.08	<u>0.2010</u>	0.8751	31.26	<u>0.2048</u>	0.8699	36.98	0.0795	0.9623
MAP-z wCAE	<u>32.01</u>	0.2441	<u>0.8717</u>	31.08	0.2205	0.8681	36.91	0.0715	<u>0.9618</u>
MAP-z wVAE V1	27.95	0.4331	0.6582	30.24	0.2201	0.8499	35.21	0.0775	0.9443
MAP-z wVAE V2	29.44	0.3088	0.8112	29.53	0.2765	0.8226	31.01	0.2660	0.8513
DiffPIR	31.98	0.1793	0.8677	30.71	0.2042	0.8492	36.08	0.0653	0.9470

Table 1: FFHQ results on diverse inverse problems: motion deblurring ($\sigma = 7.65/255$), SISR $\times 4$, inpainting with random masks.Figure 4: Qualitative image restoration results on FFHQ. From top to bottom: Gaussian deblurring ($\sigma_{blur} = 1, \sigma = 7.65/255$), SISR $\times 2$, inpainting.

indicates that these methods have a slightly different position in the perception-distortion tradeoff [61]. Visually, both methods perform very well on FFHQ.

4.3 BSD experiments

We now compare VBLE using CAEs to state-of-the-art PnP baselines on BSD dataset, which is composed of various natural images. We consider three state-of-the-art methods: DPIR [10], PnP-ADMM [8] and DiffPIR [18]. Recall that, unlike PnP methods, VBLE enables posterior sampling. Hence, we also compare to the MCMC approach PnP-ULA [33], for which 10^5 MCMC iterations are performed. For DPIR, PnP-ADMM and PnP-ULA, we use an available version of DRUNet [10] trained on BSD. For DiffPIR, a pretrained model on ImageNet [62] is used, that we finetune on BSD dataset. Similarly to FFHQ results, we provide restoration results with VBLE and its deterministic counterpart using CAE (denoted by MAPz wCAE in the experiments).

BSD Method	Deblur (Gaussian)			SISR $\times 4$			SISR $\times 2$		
	PSNR \uparrow	LPIPS \downarrow	SSIM \uparrow	PSNR \uparrow	LPIPS \downarrow	SSIM \uparrow	PSNR \uparrow	LPIPS \downarrow	SSIM \uparrow
<i>VBLE wCAE</i>	29.77	<u>0.2002</u>	<u>0.8617</u>	25.47	<u>0.3459</u>	0.6977	29.65	0.1830	0.8749
MAPz wCAE	29.28	0.2215	0.8405	<u>25.38</u>	0.3462	<u>0.6966</u>	29.65	0.1675	0.8757
<i>PnP-ULA</i>	27.71	0.2675	0.7809	24.82	0.3730	0.6894	28.42	<u>0.1659</u>	<u>0.8763</u>
DPIR	<u>29.72</u>	0.2127	0.8623	25.18	0.3652	0.6937	29.55	0.1706	0.8784
PnP-ADMM	28.96	0.2155	0.8456	24.77	0.4227	0.6659	29.31	0.1907	0.8678
DiffPIR	29.26	0.1832	0.8420	25.03	0.3164	0.6771	29.20	0.1645	0.8539

Table 2: BSD results on diverse inverse problems: Gaussian deblurring ($\sigma_{blur} = 1, \sigma = 7.65/255$), SISR $\times 4$, SISR $\times 2$. Methods in *italics* allow for posterior sampling.

Tab. 2 shows quantitative results on deblurring and SISR inverse problems, while Fig. 5 provides a visual comparison. VBLE exhibits very consistent performance as it reaches the first or second rank for a majority of inverse problems and metrics. Besides, VBLE clearly outperforms PnP-ULA, which is the only other posterior sampling method.

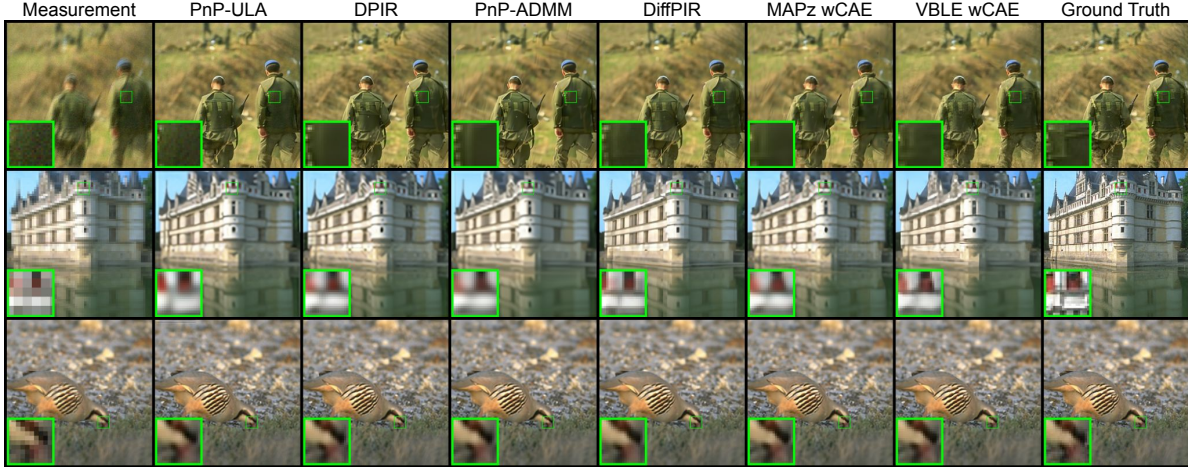
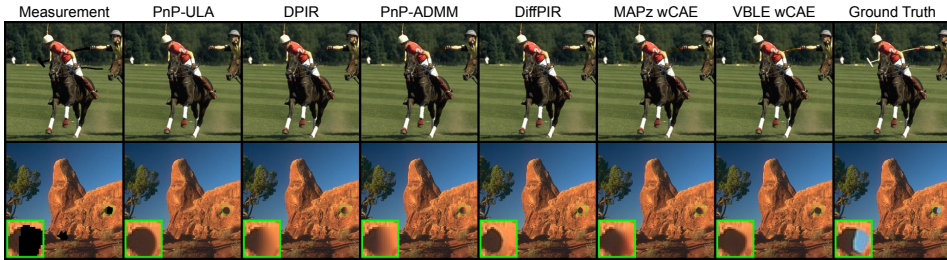


Figure 5: Qualitative image restoration results on BSD. From top to bottom: Motion deblurring ($\sigma = 7.65/255$), SISR $\times 4$, SISR $\times 2$.



DPIR	3s
DiffPIR	21s
PnP-ULA	1h23m29s
VBLE	24s
MAPz wCAE	23s

Figure 6: Left: Inpainting results on BSD, with Gaussian noise $\sigma = 2.55/255$. Right: Computational load for the different methods. Computation time is given for inpainting one BSD image on a Nvidia Quadro RTX 8000 GPU.

Visually, except for PnP-ULA, all methods perform very well. In particular, VBLE shows very relevant results, staying particularly faithful to the image. Additional inpainting with structured masks results are given in Fig. 6 together with computation times. The latter shows that VBLE wCAE is as fast as DiffPIR, slightly slower than DPIR, and several orders of magnitude faster than the other posterior sampling baseline PnP-ULA.

4.4 Posterior distribution quality assessment

Sections 4.3 and 4.2 show that VBLE using CAEs reaches state-of-the-art point estimation results for image restoration, while outperforming the MCMC method PnP-ULA. Another keypoint of VBLE is its ability to derive posterior samples and uncertainties very efficiently as variational inference enables to explicitly approximate the true posterior. Thus, we analyze in this section the quality of VBLE approximate posterior distribution.

Figure 7 shows a visual comparison of VBLE and PnP-ULA posterior samples and marginal standard deviations, estimated from posterior sampling with 100 samples. Marginal standard deviations of VBLE seem relevant and their maximum value is generally close to PnP-ULA deviations. Then for low frequency zones, VBLE exhibits low deviations in contrast to PnP-ULA. Therefore, VBLE also exhibits realistic posterior samples, while PnP-ULA ones exhibit more noise. VBLE posterior sampling ability is shown in more detail in Fig. 8. Posterior samples are sharp and realistic, showing the interest of formulating the posterior distribution in the latent space, with a uniform distribution. The MMSE-x estimate is smoother than the samples and, hence, tends to be more faithful to the target image.

5 Conclusion

In this paper, we have proposed the use of variational compressive autoencoders for regularizing imaging inverse problems. Additionally, we have introduced the VBLE algorithm which performs variational inference in the latent space of CAEs or VAEs. VBLE enables efficient approximation of the posterior distribution associated with image restoration tasks. In our experiments, compressive autoencoders, combined with VBLE, achieve state-of-the-art results

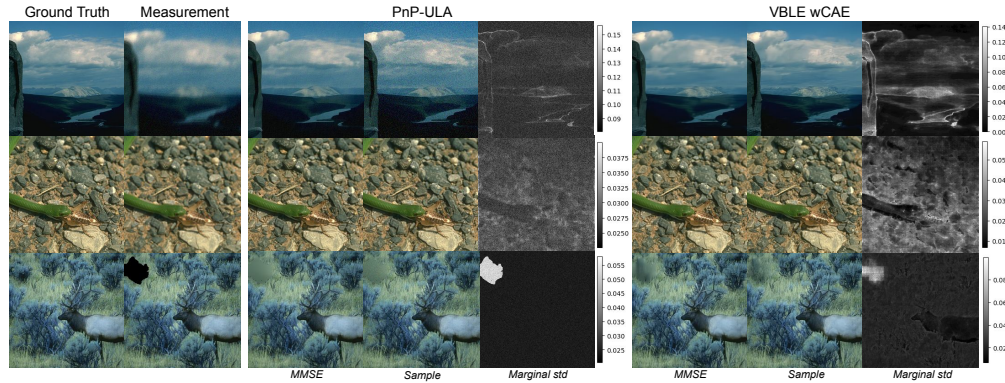


Figure 7: Visual comparison between VBLE and PnP-ULA on several inverse problems. From top to bottom: Motion deblurring ($\sigma = 7.65/255$), SISR $\times 2$, block inpainting ($\sigma = 2.55/255$).



Figure 8: Example of VBLE posterior sampling ability. The MMSE-x, which is the estimate used in all quantitative comparison, corresponds to the average over samples in the image space.

and provide compelling posterior sampling abilities. These demonstrate the interest of CAEs for image restoration as well as the possibility to estimate simply and efficiently the posterior distribution in the latent space of a generative model.

Further work will be dedicated to enhancing the performance of VBLE, by considering more expressive variational distribution families or by a joint estimation in the latent and image space [22, 23]. Another key perspective is to consider modulated CAEs [63] which allow for compression at multiple bit-rates, thus enabling the regularization of inverse problems of various difficulties with a single neural network.

Acknowledgments

This work was partly supported by CNES under project name DEEPREG, and ANITI under grant agreement ANR-19-PI3A-0004.

References

- [1] Leonid I. Rudin, Stanley Osher, and Emad Fatemi. Nonlinear total variation based noise removal algorithms. *Physica D: Nonlinear Phenomena*, 1992.
- [2] A. Tikhonov. Solution of incorrectly formulated problems and the regularization method. *Soviet Math.*, 1963.
- [3] Robert Tibshirani. Regression shrinkage and selection via the lasso. *Journal of the Royal Statistical Society: Series B (Methodological)*, 1996.
- [4] Michael Elad. *Sparse and Redundant Representations: From Theory to Applications in Signal and Image Processing*, volume 2. Springer, 2010.
- [5] Stephane Mallat. *Wavelet tour of signal processing: The sparse way*, 2008.
- [6] Chao Dong, Chen Change Loy, Kaiming He, and Xiaoou Tang. Learning a deep convolutional network for image super-resolution. *European Conference on Computer Vision (ECCV)*, pages 184–199, 2014.

- [7] Chitwan Saharia, Jonathan Ho, William Chan, Tim Salimans, David J Fleet, and Mohammad Norouzi. Image super-resolution via iterative refinement. *IEEE Transactions on Pattern Analysis and Machine Intelligence*, 45(4):4713–4726, 2022.
- [8] Singanallur V. Venkatakrishnan, Charles A. Bouman, and Brendt Wohlberg. Plug-and-play priors for model based reconstruction. *IEEE Global Conference on Signal and Information Processing (GlobalSIP)*, 2013.
- [9] Stanley H Chan, Xiran Wang, and Omar A Elgandy. Plug-and-play ADMM for image restoration: Fixed-point convergence and applications. *IEEE Transactions on Computational Imaging*, 3(1):84–98, 2016.
- [10] Kai Zhang, Yawei Li, Wangmeng Zuo, Lei Zhang, Luc Van Gool, and Radu Timofte. Plug-and-play image restoration with deep denoiser prior. *IEEE Transactions on Pattern Analysis and Machine Intelligence*, 44(10):6360–6376, 2021.
- [11] Samuel Hurault, Arthur Leclaire, and Nicolas Papadakis. Gradient step denoiser for convergent plug-and-play. In *International Conference on Learning Representations (ICLR)*, 2022.
- [12] Ulugbek S Kamilov, Hassan Mansour, and Brendt Wohlberg. A plug-and-play priors approach for solving nonlinear imaging inverse problems. *IEEE Signal Processing Letters*, 24(12):1872–1876, 2017.
- [13] Kai Zhang, Wangmeng Zuo, Shuhang Gu, and Lei Zhang. Learning deep CNN denoiser prior for image restoration. In *IEEE conference on computer vision and pattern recognition (CVPR)*, pages 3929–3938, 2017.
- [14] Jonathan Ho, Ajay Jain, and Pieter Abbeel. Denoising diffusion probabilistic models. *Advances in Neural Information Processing Systems (NeurIPS)*, 2020.
- [15] Alexander Quinn Nichol and Prafulla Dhariwal. Improved denoising diffusion probabilistic models. In *International Conference on Machine Learning (ICML)*, pages 8162–8171. PMLR, 2021.
- [16] Bahjat Kawar, Michael Elad, Stefano Ermon, and Jiaming Song. Denoising diffusion restoration models. *Advances in Neural Information Processing Systems (NeurIPS)*, 35:23593–23606, 2022.
- [17] Hyungjin Chung, Jeongsol Kim, Michael Thompson Mccann, Marc Louis Klasky, and Jong Chul Ye. Diffusion posterior sampling for general noisy inverse problems. In *International Conference on Learning Representations (ICLR)*, 2023.
- [18] Yuanzhi Zhu, Kai Zhang, Jingyun Liang, Jiezhong Cao, Bihan Wen, Radu Timofte, and Luc Van Gool. Denoising diffusion models for plug-and-play image restoration. In *IEEE/CVF Conference on Computer Vision and Pattern Recognition (CVPR)*, pages 1219–1229, 2023.
- [19] Ashish Bora, Ajil Jalal, Eric Price, and Alexandros G. Dimakis. Compressed sensing using generative models. In *International Conference on Machine Learning (ICML)*, 2017.
- [20] Manik Dhar, Aditya Grover, and Stefano Ermon. Modeling sparse deviations for compressed sensing using generative models. In *International Conference on Machine Learning (ICLR)*, pages 1214–1223. PMLR, 2018.
- [21] Joseph Dean, Giannis Daras, and Alex Dimakis. Intermediate layer optimization for inverse problems using deep generative models. In *NeurIPS 2020 Workshop on Deep Learning and Inverse Problems*, 2020.
- [22] Mario González, Andrés Almansa, and Pauline Tan. Solving inverse problems by joint posterior maximization with autoencoding prior. *SIAM Journal on Imaging Sciences*, 15(2):822–859, 2022.
- [23] Margaret Duff, Neill D. F. Campbell, and Matthias J. Ehrhardt. Regularising inverse problems with generative machine learning models. *Journal of Mathematical Imaging and Vision*, 2023.
- [24] Margaret AG Duff, Ivor JA Simpson, Matthias Joachim Ehrhardt, and Neill DF Campbell. VAEs with structured image covariance applied to compressed sensing mri. *Physics in Medicine & Biology*, 68(16):165008, 2023.
- [25] Laurent Dinh, David Krueger, and Yoshua Bengio. NICE: Non-linear independent components estimation. In *International Conference of Learning Representations (ICLR)*, 2015.
- [26] Muhammad Asim, Max Daniels, Oscar Leong, Ali Ahmed, and Paul Hand. Invertible generative models for inverse problems: mitigating representation error and dataset bias. In *International Conference on Machine Learning (ICML)*, pages 399–409. PMLR, 2020.
- [27] Thomas Oberlin and Mathieu Verm. Regularization via deep generative models: an analysis point of view. In *International Conference on Image Processing (ICIP)*, pages 404–408. IEEE, 2021.
- [28] Giannis Daras, Augustus Odena, Han Zhang, and Alexandros G Dimakis. Your local GAN: Designing two dimensional local attention mechanisms for generative models. In *IEEE/CVF conference on computer vision and pattern recognition (CVPR)*, pages 14531–14539, 2020.
- [29] Jean Prost, Antoine Houdard, Andrés Almansa, and Nicolas Papadakis. Inverse problem regularization with hierarchical variational autoencoders. In *IEEE International Conference on Computer Vision (ICCV)*, 2023.

- [30] Casper Kaae Soenderby, Tapani Raiko, Lars Maaloe, Soeren Kaae Soenderby, and Ole Winther. Ladder variational autoencoders. In D. Lee, M. Sugiyama, U. Luxburg, I. Guyon, and R. Garnett, editors, *Advances in Neural Information Processing Systems*, volume 29. Curran Associates, Inc., 2016.
- [31] Zahra Kadkhodaie and Eero Simoncelli. Stochastic solutions for linear inverse problems using the prior implicit in a denoiser. *Advances in Neural Information Processing Systems*, 34:13242–13254, 2021.
- [32] Alain Durmus, Eric Moulines, and Marcelo Pereyra. Efficient bayesian computation by proximal Markov chain Monte Carlo: when Langevin meets Moreau. *SIAM Journal on Imaging Sciences*, 11(1):473–506, 2018.
- [33] Rémi Laumont, Valentin De Bortoli, Andrés Almansa, Julie Delon, Alain Durmus, and Marcelo Pereyra. Bayesian Imaging using plug & play priors: when Langevin meets Tweedie. *SIAM Journal on Imaging Sciences*, 15(2):701–737, 2022.
- [34] Ziruo Cai, Junqi Tang, Subhadip Mukherjee, Jinglai Li, Carola Bibiane Schönlieb, and Xiaoqun Zhang. NF-ULA: Langevin Monte Carlo with Normalizing Flow Prior for Imaging Inverse Problems. *arXiv preprint arXiv:2304.08342*, 2023.
- [35] Matthew Holden, Marcelo Pereyra, and Konstantinos C. Zygalakis. Bayesian imaging with data-driven priors encoded by neural networks. *SIAM Journal on Imaging Sciences*, 15(2):892–924, 2022.
- [36] Florentin Coeurdoux, Nicolas Dobigeon, and Pierre Chainais. Plug-and-play split gibbs sampler: embedding deep generative priors in bayesian inference. *arXiv preprint arXiv:2304.11134*, 2023.
- [37] Marcelo Pereyra, Luis Vargas Miele, and Konstantinos C. Zygalakis. Accelerating Proximal Markov Chain Monte Carlo by Using an Explicit Stabilized Method. *SIAM Journal on Imaging Sciences*, 13(2):905–935, 2020.
- [38] Johannes Ballé, Valero Laparra, and Eero P. Simoncelli. End-to-end optimized image compression. In *International Conference of Learning Representations (ICLR)*, 2017.
- [39] Johannes Ballé, David Minnen, Saurabh Singh, Sung Jin Hwang, and Nick Johnston. Variational image compression with a scale hyperprior. In *International Conference of Learning Representations (ICLR)*, 2018.
- [40] Tero Karras, Samuli Laine, and Timo Aila. A style-based generator architecture for generative adversarial networks. In *IEEE/CVF conference on computer vision and pattern recognition (CVPR)*, pages 4401–4410, 2019.
- [41] D. Martin, C. Fowlkes, D. Tal, and J. Malik. A database of human segmented natural images and its application to evaluating segmentation algorithms and measuring ecological statistics. In *IEEE International Conference on Computer Vision (ICCV)*, volume 2, pages 416–423 vol.2, 2001.
- [42] Diederik P Kingma and Max Welling. Auto-encoding variational bayes. In *International Conference on Learning Representations (ICLR)*, 2014.
- [43] David M. Blei, Alp Kucukelbir, and Jon D. McAuliffe. Variational inference: A review for statisticians. *Journal of the American statistical Association*, 112(518):859–877, 2017.
- [44] Paul A Wintz. Transform picture coding. *Proceedings of the IEEE*, 60(7):809–820, 1972.
- [45] Athanassios Skodras, Charilaos Christopoulos, and Touradj Ebrahimi. The jpeg 2000 still image compression standard. *IEEE Signal processing magazine*, 18(5):36–58, 2001.
- [46] David Minnen, Johannes Ballé, and George D Toderici. Joint autoregressive and hierarchical priors for learned image compression. In *Advances in neural information processing systems (NeurIPS)*, volume 31, 2018.
- [47] Zhengxue Cheng, Heming Sun, Masaru Takeuchi, and Jiro Katto. Learned image compression with discretized gaussian mixture likelihoods and attention modules. In *IEEE Conference on Computer Vision and Pattern Recognition (CVPR)*, 2020.
- [48] Alan C Bovik. *Handbook of image and video processing*. Academic press, 2010.
- [49] Zan Chen, Wenlong Guo, Yuanjing Feng, Yongqiang Li, Changchen Zhao, Yi Ren, and Ling Shao. Deep-learned regularization and proximal operator for image compressive sensing. *IEEE Transactions on Image Processing*, 30:7112–7126, 2021.
- [50] Bin Dai and David Wipf. Diagnosing and enhancing vae models. *International Conference of Learning Representations*, 2019.
- [51] Vinicius Alves de Oliveira, Marie Chabert, Thomas Oberlin, Charly Poulliat, Mickael Bruno, Christophe Latry, Mikael Carlavan, Simon Henrot, Frederic Falzon, and Roberto Camarero. Satellite image compression and denoising with neural networks. *IEEE Geoscience and Remote Sensing Letters*, 19:1–5, 2022.
- [52] Johannes Ballé, Valero Laparra, and Eero P Simoncelli. Density modeling of images using a generalized normalization transformation. In *International Conference on Learning Representations (ICLR)*, 2016.

- [53] Francesco Tonolini, Bjørn Sand Jensen, and Roderick Murray-Smith. Variational sparse coding. 2020.
- [54] Shangqi Gao and Xiahai Zhuang. Bayesian image super-resolution with deep modeling of image statistics. *IEEE Transactions on Pattern Analysis and Machine Intelligence*, 45(2):1405–1423, 2022.
- [55] Hwan Goh, Sheroze Sherifdeen, Jonathan Wittmer, and Tan Bui-Thanh. Solving bayesian inverse problems via variational autoencoders. *arXiv preprint arXiv:1912.04212*, 2019.
- [56] Fabian Mentzer, George D Toderici, Michael Tschannen, and Eirikur Agustsson. High-fidelity generative image compression. In H. Larochelle, M. Ranzato, R. Hadsell, M.F. Balcan, and H. Lin, editors, *Advances in Neural Information Processing Systems*, volume 33, pages 11913–11924. Curran Associates, Inc., 2020.
- [57] Zhou Wang, Alan C Bovik, Hamid R Sheikh, and Eero P Simoncelli. Image quality assessment: from error visibility to structural similarity. *IEEE transactions on image processing*, 13(4):600–612, 2004.
- [58] Richard Zhang, Phillip Isola, Alexei A. Efros, Eli Shechtman, and Oliver Wang. The unreasonable effectiveness of deep features as a perceptual metric. In *IEEE/CVF Conference on Computer Vision and Pattern Recognition (CVPR)*, pages 586–595, 2018.
- [59] Jean Bégaint, Fabien Racapé, Simon Feltman, and Akshay Pushparaja. CompressAI: a PyTorch library and evaluation platform for end-to-end compression research. *arXiv preprint arXiv:2011.03029*, 2020.
- [60] Jooyoung Choi, Sungwon Kim, Yonghyun Jeong, Youngjune Gwon, and Sungroh Yoon. ILVR: Conditioning method for denoising diffusion probabilistic models. In *IEEE/CVF International Conference on Computer Vision (ICCV)*, pages 14347–14356, 2021.
- [61] Yochai Blau and Tomer Michaeli. The perception-distortion tradeoff. In *Proceedings of the IEEE conference on computer vision and pattern recognition*, pages 6228–6237, 2018.
- [62] Prafulla Dhariwal and Alexander Nichol. Diffusion models beat GANs on image synthesis. *Advances in Neural Information Processing Systems (NeurIPS)*, 34:8780–8794, 2021.
- [63] Myungseo Song, Jinyoung Choi, and Bohyung Han. Variable-rate deep image compression through spatially-adaptive feature transform. In *IEEE/CVF International Conference on Computer Vision (ICCV)*, pages 2380–2389, 2021.

Supplementary Material

A Ablation Study

For the experiments presented in the paper, some choices have been made. In particular, the MMSE-x estimate has been preferred to the MMSE-z estimate (see Sec. 3.2), while only z has been optimized as we approximated the second latent variable $h = E_{h,\phi}(\tilde{z})$ (see Sec. 3.1). In this section, in order to justify these choices, quantitative and qualitative results with the MMSE-z estimate and with an optimization on (z, h) (denoted $\text{VBLE}_{z,h}$) are given in Tab. 3 and in Fig. 9.

All these compared variants of the proposed method share the same restoration parameters (*i.e.* same λ and α) and use the same CAE.

Method	FFHQ - SISR $\times 4$			BSD - Gaussian deblur		
	PSNR \uparrow	LPIPS \downarrow	SSIM \uparrow	PSNR \uparrow	LPIPS \downarrow	SSIM \uparrow
VBLE MMSE-x	31.44	0.2032	0.8732	24.55	0.4030	0.6346
VBLE MMSE-z	31.39	0.2296	0.8714	24.60	0.4446	0.6409
VBLE $_{z,h}$ MMSE-x	31.44	0.2021	0.8732	24.55	0.4062	0.6346

Table 3: Quantitative results for different variants of our method. MMSE-x and MMSE-z denote the two possible estimators defined in Sec. 3.2. For the Gaussian deblur experiment, $\sigma = 7.65/255$ and $\sigma_k = 3$.



Figure 9: Visual results for different variants of our method. Top: SISR $\times 4$. Bottom: Gaussian deblurring ($\sigma_k = 3$, $\sigma = 7.65/255$).

First, the optimization on (z, h) does not perform better than the optimization on z only. For that reason, we choose to optimize only on z for the main experiments, as the formulation is much simpler. Furthermore, the MMSE-z estimate yields similar PSNR and SSIM results as the MMSE-x estimate, but exhibits always a poorer LPIPS.

Additionally, a study on VBLE hyperparameters α (bitrate parameter) and λ (regularization parameter) is provided in Fig. 10. Parameter λ seems a more sensitive parameter than α , hence a CAE with a single bitrate could solve a wide range of inverse problem. Furthermore, the prior on FFHQ seems to be more informative compared to the one on BSD, which makes sense as BSD dataset structure is much harder to learn.



Figure 10: Influence of hyperparameters λ (regularization parameter) and α (bitrate parameter) on VBLE algorithm. To the left, on a deblurring problem on a BSD image, to the right, on a SISR problem on a FFHQ image.

B Detailed experimental setup

B.1 Compressive autoencoders details

In the main paper, the CAE from Cheng et al. [47], denoted as cheng in the following, has been used in all experiments, for simplicity. Here, we also provide results using Minnen et al. [46] CAE, denoted as mbt. As cheng, mbt is a CAE with an hyperprior combining a second autoencoder with an autoregressive model. However, its encoder and decoder structures remain simple CNNs, in contrast to cheng, which has deeper and more elaborate encoder and decoder.

As for cheng model, we employ pretrained networks from the compressAI [59] library at different bitrates, that we finetune for about 100k iterations on BSD and FFHQ train datasets.

B.2 VAE architecture details

VAE-V1 and V2 models, used for Bora et al. [19] baseline on FFHQ, are vanilla VAEs, that is VAEs with a single latent variable. Their structure has been designed so that it has same depth, hidden channels and latent dimension as mbt with (respectively without) hyperprior in the case of VAE-V1 (respectively VAE-V2). Hence, VAE-V1 encoder possesses 5 convolutional layers, four of them with a stride of 2. VAE-V2 has 7 convolutional layers, six of them with a stride of 2. Batch Normalization and Leaky Relu activations are used. The decoder structures are symmetric. The latent dimension is $192 \times 16 \times 16$ for VAE-V1 and $192 \times 4 \times 4$ for VAE-V2, assuming 256×256 images. These dimensions correspond to z (first latent variable) and h (second latent variable) sizes of mbt CAE.

Both models have been trained on FFHQ using a learning rate of $1e - 4$ during at least 300k iterations. We choose a Gaussian assumption for the decoder, that is $p_{\theta}(x|z) = \mathcal{N}(D_{\theta}(z), \gamma^2 I)$. The variance γ^2 is considered as a global parameter and is learned with the other network parameters.

The number of parameters of these VAEs, as well as of the other models used for the image restoration experiments, are detailed in Tab. 4. In particular, VAE-V2 has approximately the same number of parameters as the low bitrate version of mbt because the two networks have same size (but VAE-V2 does not include an autoregressive module). VAE-V1 has slightly fewer parameters as its structure imitates mbt without the hyperprior module.

B.3 Detailed experimental settings for image restoration

To tune image restoration hyperparameters of VBLE and of the baselines, a grid search algorithm has been used on a separate 3 image sets of FFHQ and BSD test datasets. Tab. 5 identifies the parameters which have been tuned or the one that have been fixed, for each method. Furthermore, precise parameter settings for VBLE are available in Tab. 6.

Dataset	DRUNet	Diffusion model	VAE-V1	VAE-V2	CAE cheng	CAE mbt
BSD	32M	93M	x	x	29M	14-25M
FFHQ	x	552M	8.3M	12M	29M	14-25M

Table 4: Number of parameters of the neural network used for VBLE and the baselines. For mbt number of parameters, 14M correspond to low bitrate networks, 25M to high bitrates.

Method	Optimized parameters	Fixed parameters
VBLE wCAE	- λ (regularization) - α (bitrate)	- 1000 iterations
MAPz wCAE	- λ (regularization) - α (bitrate)	- 1000 iterations
DPIR	- λ (regularization) - number of iterations	x
PnP-ADMM	- λ (regularization) - number of iterations - denoiser noise	x
PnP-ULA	- λ (regularization) - denoiser noise - step size of the Markov Chain	- 10^5 iterations - Thinning 200 - Burn-in 0.8
DiffPIR	- λ (regularization) - ζ	- 100 diffusion iterations
MAPz wVAE (Bora et al.)	- λ (regularization)	- 500 iterations

Table 5: Detailed experimental settings for VBLE and the baselines.

BSD	Deblur $\sigma = 2.55/255$			Deblur $\sigma = 7.65/255$			SISR		Inpainting	
	$\sigma_k = 1$	$\sigma_k = 3$	Motion	$\sigma_k = 1$	$\sigma_k = 3$	Motion	$\times 2$	$\times 4$	50%	
cheng	α	0.0932	0.0067	0.0483	0.0067	0.0035	0.0067	0.025	0.0035	0.1800
	λ	8.7	19.2	9.1	82.0	81.4	75.4	5.8	8.5	20.4
mbt	α	0.0483	0.0067	0.025	0.0067	0.0035	0.0067	0.025	0.0067	0.0932
	λ	9.5	10.7	8.2	76.2	66.5	71.2	4.7	6.9	9.2

FFHQ	Deblur $\sigma = 2.55/255$			Deblur $\sigma = 7.65/255$			SISR		Inpainting	
	$\sigma_k = 1$	$\sigma_k = 3$	Motion	$\sigma_k = 1$	$\sigma_k = 3$	Motion	$\times 2$	$\times 4$	50%	
cheng	α	0.1800	0.0067	0.0932	0.025	0.0035	0.025	0.0483	0.0.013	0.1800
	λ	7.5	24.3	8.6	82.5	142.8	72.7	1.4	1.6	10.8
mbt	α	0.0932	0.0067	0.0483	0.013	0.0035	0.0067	0.0483	0.013	0.0932
	λ	8.9	7.8	8.1	82.9	73.6	64.8	1.1	0.62	6.2

Table 6: Detailed parameter setting for VBLE using cheng and mbt compressive networks, for all experiments in the paper. λ is the regularization parameter and α the bitrate parameter. Specifically, each CAE is trained with the loss $\mathcal{L} = 255^2 \alpha \text{Distortion} + \text{Rate}$. For mbt and cheng models, two structures, a light and a bigger one, exist [59], which are used respectively for low and high bitrates. For mbt, high bitrate structure is used for $\alpha \geq 0.013$, and low bitrate structure for $\alpha \leq 0.0067$. For cheng, we have chosen the high bitrate structure for high and low bitrates, as it provides the best image restoration results.

C Additional experimental results

C.1 FFHQ additional results

Complete FFHQ quantitative results are given in Tab. 7, including all inverse problems and methods which were tested.

In particular, it includes our method using mbt CAE (denoted as VBLE and MAPz wCAE (mbt)), which permits the most relevant comparison to Bora et al. [19] method (MAPz wVAE) using VAE-V1 and V2 as these networks have

SISR and Inp. Method	SISR $\times 2$			SISR $\times 4$			Inpainting (random)		
	PSNR \uparrow	LPIPS \downarrow	SSIM \uparrow	PSNR \uparrow	LPIPS \downarrow	SSIM \uparrow	PSNR \uparrow	LPIPS \downarrow	SSIM \uparrow
VBLE wCAE	36.32	0.0995	0.9516	31.26	<u>0.2048</u>	0.8699	<u>36.98</u>	0.0795	0.9623
MAP-z wCAE	<u>36.30</u>	0.0995	0.9516	<u>31.08</u>	0.2205	<u>0.8681</u>	36.91	0.0715	0.9618
VBLE wCAE (mbt)	35.99	<u>0.0956</u>	0.9514	31.01	0.2258	0.8680	37.04	0.0738	0.9643
MAP-z wCAE (mbt)	35.85	0.0812	0.9507	30.05	0.2421	0.8386	36.25	0.0528	<u>0.9628</u>
MAP-z wVAE V1	34.35	0.0893	0.9311	30.24	0.2201	0.8499	35.21	0.0775	0.9443
MAP-z wVAE V2	31.20	0.2592	0.8534	29.53	<u>0.2765</u>	0.8226	31.01	0.2660	0.8513
DiffPIR	34.94	0.1089	0.9269	30.71	0.2042	0.8492	36.08	<u>0.0653</u>	0.9470
Deblur - $\sigma = 7.65$									
Method	Gaussian, $\sigma_k = 1$			Gaussian, $\sigma_k = 3$			Motion		
	PSNR \uparrow	LPIPS \downarrow	SSIM \uparrow	PSNR \uparrow	LPIPS \downarrow	SSIM \uparrow	PSNR \uparrow	LPIPS \downarrow	SSIM \uparrow
VBLE wCAE	34.34	<u>0.1440</u>	0.9186	29.49	<u>0.2755</u>	0.8183	32.08	<u>0.2010</u>	0.8751
MAP-z wCAE	34.17	0.1684	0.9152	<u>29.44</u>	0.2977	<u>0.8176</u>	<u>32.01</u>	0.2441	0.8717
VBLE wCAE (mbt)	<u>34.21</u>	0.1600	<u>0.9177</u>	28.70	0.3212	0.7686	31.97	0.2149	<u>0.8741</u>
MAP-z wCAE (mbt)	34.02	0.1822	0.9104	29.33	0.3076	0.8124	31.31	0.2647	0.8529
MAP-z wVAE V1	32.78	0.1990	0.8868	28.72	0.3242	0.7961	27.95	0.4331	0.6582
MAP-z wVAE V2	30.91	0.2688	0.8486	28.47	0.3263	0.7849	29.44	0.3088	0.8112
DiffPIR	33.92	0.1368	0.9049	29.41	0.2691	0.8102	31.98	0.1793	0.8677
Deblur - $\sigma = 2.55$									
Method	Gaussian, $\sigma_k = 1$			Gaussian, $\sigma_k = 3$			Motion		
	PSNR \uparrow	LPIPS \downarrow	SSIM \uparrow	PSNR \uparrow	LPIPS \downarrow	SSIM \uparrow	PSNR \uparrow	LPIPS \downarrow	SSIM \uparrow
VBLE wCAE	36.92	0.0834	0.9518	30.29	<u>0.2443</u>	0.8429	35.86	0.1118	0.9371
MAP-z wCAE	36.69	0.0983	0.9483	<u>30.42</u>	0.2641	0.8445	35.55	0.1272	0.9321
VBLE wCAE (mbt)	<u>36.73</u>	<u>0.0864</u>	<u>0.9503</u>	30.28	0.2607	0.8362	<u>35.76</u>	0.1169	<u>0.9358</u>
MAP-z wCAE (mbt)	36.72	0.0980	0.9489	30.13	0.2700	0.8348	34.81	0.1626	0.9138
MAP-z wVAE V1	34.96	0.1179	0.9283	29.91	0.2743	0.8291	32.91	0.1832	0.8926
MAP-z wVAE V2	31.05	0.2618	0.8511	29.00	0.3008	0.8042	29.88	0.2864	0.8236
DiffPIR	36.08	0.0900	0.9356	30.75	0.2149	<u>0.8437</u>	34.88	<u>0.1135</u>	0.9155

Table 7: FFHQ results on diverse inverse problems. For methods using CAEs, (mbt) means that mbt CAE [46] is used, otherwise cheng CAE [47] is used.

comparable size (see appendix B.2). MAP-z wVAE remains a large margin below MAP-z wCAE (mbt), even on problems for which a low bitrate version of mbt is used (for instance, motion deblur ($\sigma = 7.65$) and Gaussian deblur ($\sigma_k = 3, \sigma = 2.55$)). Hence, it confirms the interest of using the two latent structure of CAEs, as mentioned in the main paper. It is worth noting that a VAE having the same two latent variable structure than the mentioned CAEs is likely to perform as well as CAEs, although such a network may not be straightforward to design. Indeed, VAE and CAE formulations deviate because of the autoregressive module used for the hyperprior.

Furthermore, mbt CAE slightly underperforms cheng for image restoration. It seems meaningful as mbt is shallower. However, it provides a faster version of VBLE using CAEs as the restoration process takes 11s instead of 24s for cheng model, for 1000 iterations on an inpainting problem, using the same GPU and CPUs.

Additional visual results are given in Fig. 11.



Figure 11: FFHQ additional visual results

C.2 BSD additional results

Additional quantitative results are given on BSD dataset in Tab. 8, as well as extensive visual comparison between our method and the baselines in Fig. 12.

BSD		Deblur (Gauss., $\sigma_k = 3$)			Deblur (Motion)			Inpainting (Random)		
Method	PSNR \uparrow	LPIPS \downarrow	SSIM \uparrow	PSNR \uparrow	LPIPS \downarrow	SSIM \uparrow	PSNR \uparrow	LPIPS \downarrow	SSIM \uparrow	
<i>VBLE wCAE</i>	<u>24.55</u>	<u>0.4030</u>	0.6346	<u>28.56</u>	<u>0.2466</u>	<u>0.8163</u>	30.45	0.1247	0.9091	
<i>MAPz wCAE</i>	24.48	0.4193	0.6347	28.07	0.3111	0.7896	30.12	0.1208	0.9061	
<i>PnP-ULA</i>	23.75	0.4592	0.5913	27.17	0.2643	0.7402	26.29	0.2497	0.8122	
DPIR	24.41	0.4315	0.6427	28.69	0.2606	0.8285	<u>31.58</u>	0.0659	<u>0.9316</u>	
PnP-ADMM	24.24	0.4350	0.6333	28.16	0.3349	0.8045	31.69	<u>0.0675</u>	0.9322	
DiffPIR	24.58	0.3605	<u>0.6405</u>	28.15	0.2230	0.7955	30.41	0.0919	0.9018	

Deblur - $\sigma = 2.55$		Gaussian, $\sigma_k = 1$			Gaussian, $\sigma_k = 3$			Motion		
Method	PSNR \uparrow	LPIPS \downarrow	SSIM \uparrow	PSNR \uparrow	LPIPS \downarrow	SSIM \uparrow	PSNR \uparrow	LPIPS \downarrow	SSIM \uparrow	
<i>VBLE wCAE</i>	<u>32.05</u>	<u>0.1234</u>	<u>0.9152</u>	<u>25.21</u>	<u>0.3676</u>	0.6738	32.37	0.1392	0.9112	
<i>MAPz wCAE</i>	31.45	0.1450	0.9025	25.16	0.3723	0.6753	32.01	0.1668	0.9011	
<i>PnP-ULA</i>	30.03	0.1751	0.8707	24.60	0.4027	0.6430	31.64	0.1304	0.8941	
DPIR	32.25	0.1307	0.9187	25.12	0.3809	0.6838	33.07	<u>0.1305</u>	0.9237	
PnP-ADMM	31.21	0.1381	0.9049	24.12	0.3991	0.6667	<u>32.92</u>	0.1483	<u>0.9192</u>	
DiffPIR	31.78	0.1131	0.9045	25.30	0.3172	<u>0.6783</u>	31.80	0.1242	0.8936	

Table 8: Additional BSD results on diverse inverse problems. Top: for deblur problems, $\sigma = 7.65/255$. Bottom: for deblur problems, $\sigma = 2.55/255$.



Figure 12: BSD additional visual results

C.3 Uncertainties and posterior sampling evaluation

Additional visual results assessing the quality of VBLE posterior sampling are shown in Fig. 13.

Furthermore, Sec. 4.4 consists in an evaluation of VBLE posterior sampling ability. The marginal variances for VBLE are visually compared to PnP-ULA ones. Note that, as in MCMC image restoration papers [33, 35, 36], their quality is not quantitatively assessed. Indeed, a rigorous approach would require a metric that evaluates the quantity of information contained in the posterior as a whole. This appears to be complex and such metrics have, to our knowledge, not been developed for imaging problems.

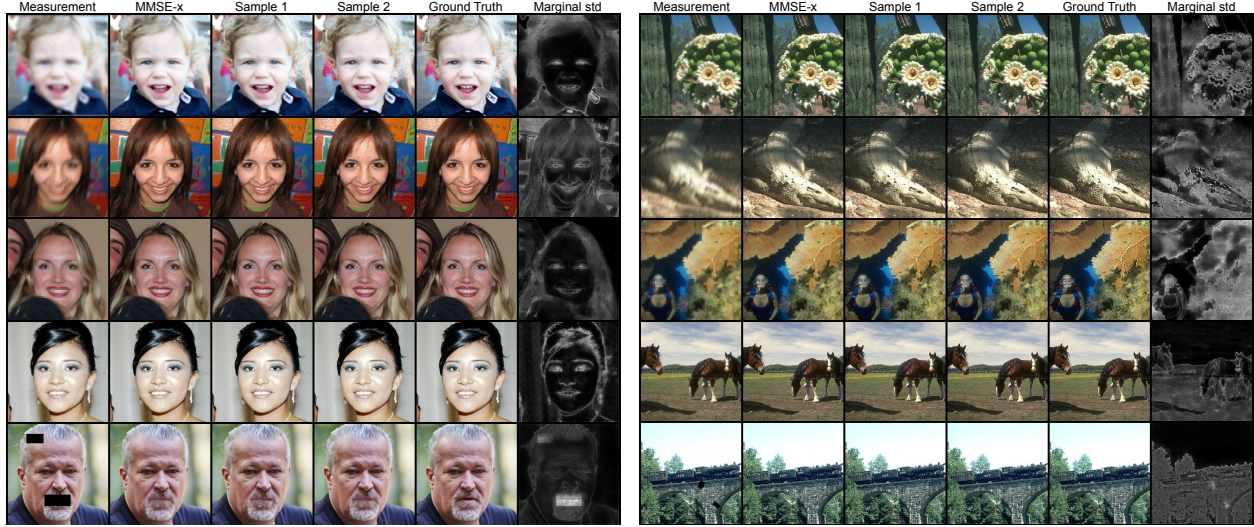


Figure 13: Posterior sampling visualisation for VBLE (cheng) for several inverse problems on BSD and FFHQ datasets.

Nevertheless, for VBLE, it seems of particular importance to assess the relevance of the produced uncertainties, as the obtained posterior, in contrast to MCMC, is an approximation of the true posterior. Therefore, we choose to use an empirical way to evaluate marginal variances.

The evaluation method consists in ensuring the consistency of the predicted marginal variances, for the given approximated posterior mean. Specifically, after applying the VBLE algorithm, $q_{z^*, a^*}(z)$ approximates $p_{Z|Y}(z|y)$. Then, we choose to model $p_{X|Y}(x|y)$ by a Gaussian distribution $p^*(x|y)$ whose parameters are estimated by posterior sampling, assuming the independence of each pixel. Hence,

$$p^*(x|y) = \mathcal{N}(x; x_{MMSE-x}^*, \Sigma^{img}) \quad (14)$$

where Σ^{img} is a diagonal matrix containing the marginal variances of each pixel of the image. Hence, if $p^*(x|y)$ is a good approximation of $p_{X|Y}(x|y)$, the ideal image x should follow $p^*(x|y)$. A classical metrics to evaluate that is the negative log-likelihood defined by

$$NLL = -\log \mathcal{N}(x; x_{MMSE-x}^*, \Sigma^{img}). \quad (15)$$

The NLL will thus increase if $p^*(x|y)$ does not correctly model the image x . It is worth noting that a posterior distribution yielding a poor MMSE estimate but adapted marginal variances get a decent NLL. Hence, this metrics mainly evaluates the calibration of the marginal variances given the MMSE estimation, thus being complementary to a point quality metrics such as PSNR or LPIPS.

Dataset	Method	Deblur $\sigma = 2.55$			Deblur $\sigma = 7.65$			SISR		Inpainting
		Gaussian $\sigma_k = 1$	Gaussian $\sigma_k = 3$	Motion	Gaussian $\sigma_k = 1$	Gaussian $\sigma_k = 3$	Motion	$\times 2$	$\times 4$	50 %
BSD	VBLE	3.86	4.40	3.85	3.59	4.07	3.84	5.61	4.27	5.44
	PnP-ULA	3.74	4.29	3.29	3.88	4.37	4.03	4.79	8.84	3.33
FFHQ	VBLE	2.62	3.30	2.85	2.79	3.35	3.04	4.27	3.43	3.28
	PnP-ULA	3.03	3.72	3.65	3.49	3.99	3.75	3.16	5.19	2.00

Table 9: Negative Log-likelihood (NLL \downarrow) scores for VBLE (cheng model) and PnP-ULA on various inverse problems.

Tab. 9 shows the NLL of VBLE and PnP-ULA posterior distribution for several inverse problems. VBLE yields similar or better NLL than PnP-ULA in deblurring and SISR, while PnP-ULA has better NLL scores in inpainting. These results confirm the observations of Sec. 4.4 and show the relevance of VBLE uncertainties.